Metrologia

Predictable quantum efficient detector based on *n*-type silicon photodiodes

OPEN ACCESS
IOP Publishing | Bureau International des Poids et Mesures Metrologia
Metrologia **54** (2017) 821–836 https://doi.org/10.1088/1681-7575/aa85ed

Predictable quantum efficient detector based on *n*-type silicon photodiodes

Timo Dönsberg[1], Farshid Manoocheri[1], Meelis Sildoja[1,10], Mikko Juntunen[1,11], Hele Savin[1], Esa Tuovinen[2], Hannu Ronkainen[2], Mika Prunnila[2], Mikko Merimaa[2], Chi Kwong Tang[3], Jarle Gran[3], Ingmar Müller[4], Lutz Werner[4], Bernard Rougié[5], Alicia Pons[6], Marek Smîd[7], Péter Gál[8], Lapo Lolli[9], Giorgio Brida[9], Maria Luisa Rastello[9] and Erkki Ikonen[1,2]

[1] Aalto University, PO Box 13000, 00076 Aalto, Finland
[2] VTT Technical Research Centre of Finland Ltd, PO Box 1000, 02044 VTT, Finland
[3] Justervesenet, PO Box 170, 2027 Kjeller, Norway
[4] Physikalisch-Technische Bundesanstalt (PTB), Abbestr. 2-12, 10587 Berlin, Germany
[5] Laboratoire Commun de Métrologie LNE-CNAM, 61 Rue du Landy, 93210 Saint Denis, France
[6] Consejo Superior de Investigaciones Científicas (CSIC), c/Serrano 144, Madrid 28006, Spain
[7] Český metrologický institute (CMI), LFM, V Botanice 4, Praha 5, Czech Republic
[8] Magyar Kereskedelmi Engedélyezési Hivatal (MKEH), Németvölgyi út 37-39, 1124 Budapest, Hungary
[9] Istituto Nazionale di Ricerca Metrologica (INRIM), Strada delle Cacce 91, 10135 Torino, Italy

E-mail: timo.donsberg@aalto.fi

Received 8 June 2017, revised 9 August 2017
Accepted for publication 14 August 2017
Published 4 October 2017

Abstract

The predictable quantum efficient detector (PQED) consists of two custom-made induced junction photodiodes that are mounted in a wedged trap configuration for the reduction of reflectance losses. Until now, all manufactured PQED photodiodes have been based on a structure where a SiO_2 layer is thermally grown on top of *p*-type silicon substrate. In this paper, we present the design, manufacturing, modelling and characterization of a new type of PQED, where the photodiodes have an Al_2O_3 layer on top of *n*-type silicon substrate. Atomic layer deposition is used to deposit the layer to the desired thickness. Two sets of photodiodes with varying oxide thicknesses and substrate doping concentrations were fabricated. In order to predict recombination losses of charge carriers, a 3D model of the photodiode was built into Cogenda Genius semiconductor simulation software. It is important to note that a novel experimental method was developed to obtain values for the 3D model parameters. This makes the prediction of the PQED responsivity a completely autonomous process. Detectors were characterized for temperature dependence of dark current, spatial uniformity of responsivity, reflectance, linearity and absolute responsivity at the wavelengths of 488 nm and 532 nm. For both sets of photodiodes, the modelled and measured responsivities were generally in agreement within the measurement and modelling uncertainties of around 100 parts per million (ppm). There is, however, an indication that the modelled internal quantum deficiency may be underestimated by a similar amount. Moreover, the responsivities of the detectors were spatially

[10] Present address: Physikalisch-Technische Bundesanstalt (PTB), Braunschweig, Germany.
[11] Present address: Institute of Physics, University of Helsinki, Helsinki, Finland.

uniform within 30 ppm peak-to-peak variation. The results obtained in this research indicate that the *n*-type induced junction photodiode is a very promising alternative to the existing *p*-type detectors, and thus give additional credibility to the concept of modelled quantum detector serving as a primary standard. Furthermore, the manufacturing of PQEDs is no longer dependent on the availability of a certain type of very lightly doped *p*-type silicon wafers.

Keywords: radiometry, induced junction, silicon photodetector, primary standard, radiant flux

(Some figures may appear in colour only in the online journal)

1. Introduction

Recently the concept of predictable quantum efficient detector (PQED) was introduced as a straightforward method of accurate radiant flux measurements in the visible wavelength range [1–3], and also included as one of the methods to quantify the amount of incident optical radiation in the *mise en pratique* of the candela [4]. In general, the radiometric quantity radiant flux [5–7], commonly referred to as optical power, can be realized using absolute radiation sources or detectors. Source-based realization of the absolute radiant power scale can be based on Planckian radiators [6–8], synchrotron radiation [6, 7, 9–11], or photon pairs produced by parametric down-conversion [7, 12, 13]. Standard detectors, on the other hand, can be divided into two main categories based on their operation principle: thermal detectors sense the heating effect of optical radiation and quantum detectors, such as silicon photodiodes, convert photons into detected charge carriers. In detector-based radiometry, the cryogenic electrical substitution radiometer (ESR) [6, 7, 14–18] has been a pivotal instrument since its inception around the turn of the 1980s, enabling unprecedented low uncertainties typically around 100 parts per million (ppm) [19] and for certain calibration conditions as low as 30 ppm [2]. Consequently, over a wide spectral range, the absolute radiant power scales of most National Metrology Institutes (NMIs) are traceable to cryogenic ESRs [20, 21]. However, these instruments are operated near the temperature of 10 K, and have demerits, such as high investment and maintenance costs, demanding operation, relatively small dynamic range and slow response.

The other category of standard detectors consists of quantum detectors. For an ideal quantum detector, the conversion ratio of incident photons into electron–hole pairs is exactly one; thus, the spectral responsivity

$$R_0(\lambda) = \frac{e\lambda}{hc} \tag{1}$$

is only dependent on the vacuum wavelength λ and fundamental constants c, e and h. In practice, however, the responsivity is affected by reflectance of the detector, $\rho(\lambda)$, and relative losses and gains of the charge carriers in the photodiode, $\delta(\lambda)$. Therefore, the spectral responsivity of a practical silicon photodiode is given by

$$R(\lambda) = R_0(\lambda)\,(1-\rho(\lambda))\,(1-\delta(\lambda)), \tag{2}$$

where the latter parameter $\delta(\lambda)$, also referred to as internal quantum deficiency (IQD), can be further divided into components arising from recombination losses and quantum gains of charge carriers and absorption losses of photons. The combined effect of IQD and reflectance losses is called external quantum deficiency (EQD). Predicting the value of $\delta(\lambda)$ using fundamental principles together with the knowledge of some physical parameters enables to use the silicon photodiode as an absolute radiometric standard. This concept was first proposed in the late 1970s [22] and studied during the following decade [23–28]. However, it was not until quite recently that uncertainties close to those of cryogenic ESRs were proposed [29] and achieved [1–3]. Gran and Sudbø developed the technique of hybrid self-calibration [30, 31], which combines the self-calibration method by Zalewski and Geist [23] and an absolute calibration method of silicon photodiodes by purely relative measurements [32]. With the hybrid self-calibration, responsivity of a trap detector employing commercial photodiodes can be determined with standard uncertainty around 200 ppm at the wavelength range of 600 nm–900 nm [30, 31].

The motivation behind the PQED [1–3, 33, 34] is to reduce both loss mechanisms $\rho(\lambda)$ and $\delta(\lambda)$, so that their magnitude can be determined with small enough uncertainty. The near-zero IQD of the PQED is achieved by using custom-made induced junction photodiodes [1, 35]. Using a one-dimensional (1D) photodiode model, the IQD has been predicted with an estimated standard uncertainty of 70 ppm in the visible wavelength range [33]. Further work to improve the prediction using three-dimensional (3D) modelling has been on-going [36]. Reflectance losses, on the other hand, are controlled using the trap configuration [1, 37, 38], which reduces the specular reflection to tens of ppm for *p* polarized light. The diffuse reflectance of the custom-made photodiodes has been measured to be less than 0.05 ppm [1]. In order to prevent dust and moisture contamination, the detectors are assembled in a clean room, and room temperature operation is done using dry nitrogen flow [3]. The combined standard uncertainty of the responsivity in the visible wavelength range is less than 100 ppm. This result has been experimentally confirmed with measurements against cryogenic ESRs [2]. The comparison between measured and predicted spectral responsivities of *p*-type PQEDs showed systematic underestimations of the EQD between 11 ppm at 476 nm and 111 ppm at 760 nm at room temperature [1, 2]. This means, however, that the prediction and experimental validation agree at the 95% confidence level.

The PQED has the potential to serve as a primary standard of optical power. It has many advantages over primary methods discussed above, such as low investment and maintenance cost, compact size and convenience of use similar

to typical trap detectors. Moreover, its responsivity is linear over seven orders of magnitude [2] and provides uncertainties comparable to the cryogenic ESR even when it is operated at room temperature. In addition to radiometry, the PQED has been exploited in photometry [39, 40], and it is also listed as a primary method in the *mise en pratique* for the definition of the candela and associated derived units [4]. Other applications include fibre optic power measurements [41] and absolute radiation thermometry [42]. There is also an on-going research to operate the induced junction photodiode of the PQED both as a thermal and as a quantum detector [43–46], thus combining two independent primary standard detectors into one device. Disadvantages of the PQED are the limited wavelength range and high demand of cleanliness in the manufacturing and assembly, and the lack of procedure to validate some of the assumptions made in the prediction of the PQED responsivity. In addition, two of the parameters used in predicting the responsivity, bulk lifetime of the charge carriers and effective surface recombination velocity of charge carriers, have been problematic as they can only be estimated with relatively high uncertainty [33].

Until now, all manufactured PQEDs have been based on induced junction photodiodes, where a silicon dioxide (SiO_2) layer of 200 nm–300 nm in thickness is thermally grown on top of *p*-type silicon substrate. This structure inherently contains trapped positive charge close to the Si–SiO_2 boundary [47], which generates an *n*-type inversion layer in the *p*-type silicon and produces a depletion region required for photocurrent generation [1, 35]. The manufacturing process described in [1] has the drawback that growing sufficiently thick SiO_2 takes long time. Due to operation at temperatures around 1000 °C, the process is also expensive and increases the risk of contamination. Moreover, the manufacturing of PQEDs is dependent on the availability of very lightly doped *p*-type silicon oriented in ⟨1 1 1⟩ direction. The detector industry, on the other hand, uses predominantly *n*-type silicon substrates.

Induced junction photodiodes can also be manufactured using *n*-type silicon substrate, which requires negative charge to be present in the oxide layer in order to form the inversion layer. This can be achieved, for example, with an aluminium oxide (Al_2O_3) layer on top of the substrate, for which negative surface charges around 10^{13} e cm^{-2} have been observed [48]. Moreover, the oxide layer can be grown using atomic layer deposition (ALD) [49, 50], which provides a controlled method to produce uniform oxide layers to an atomically specified thickness. This approach of *n*-type induced junction with ALD grown Al_2O_3 layer has been demonstrated to work as quantum detector with IQD less than 3.4% at 490 nm [51] and later the same idea was exploited in manufacturing broadband black silicon photodiodes with EQD less than 4% over the wavelength range of 250–950 nm [52].

In this work, we introduce a new type of PQED photodiode, where ALD is used to grow an Al_2O_3 layer on top of *n*-type silicon substrate. The fundamental structure of the new photodiode is similar to the previous design [1], but due to the high fixed charge density Q_f, the Al_2O_3 layer can be a factor of 10 thinner than the SiO_2 layers used with *p*-type PQED photodiodes. Two sets of photodiodes were manufactured using substrates with varying doping concentrations and thicknesses and assembled into PQED trap configurations. For both sets, the responsivities of the detectors were predicted by determining the absorption, reflectance and recombination losses. The refractive index and absorption coefficient of the Al_2O_3 layer and the layer thicknesses of the photodiode structure were measured using spectroscopic ellipsometry. The obtained values were used to calculate absorption and reflectance losses using the transfer-matrix method (TMM). Reflectance losses were also measured from the backreflected beam of the PQED. In addition, detectors were characterized for temperature dependence of dark current, spatial uniformity of responsivity and photocurrent ratio, linearity, and absolute responsivity. In order to estimate recombination losses, a 3D simulation model of the photodiode structure was built into the semiconductor simulation software Cogenda Genius TCAD v. 1.8.0 [53]. With the exception of surface recombination velocity for electrons and holes, S_0, and fixed charge of the Al_2O_3 layer, the modelling parameters that cannot be arbitrarily selected in the manufacturing process were obtained from the wafer manufacturer or directly measured. We developed a new method to extract the values for the parameters S_0 and Q_f, where simulated relative changes of the photocurrent as a function of bias voltage are compared with the experimental data. This makes the prediction of the PQED responsivity a completely autonomous process.

2. Photodiodes and detector assembly

Theory and physical properties of the induced-junction photodiodes are discussed, for example, in [1, 35, 54]. While these studies assume a structure of a SiO_2 layer on a *p*-type Si substrate, the system is described in terms of charge distributions, and thus the theory is also applicable to the *n*-type Si with an Al_2O_3 layer. Hence, our main focus is in the design and processing of the photodiodes and theory is discussed only briefly.

2.1. Photodiode structure

Figure 1 shows the schematic cross section of the *n*-type induced junction photodiode design. With the exception of opposite dopants, oxide layer material, and back-side diode contact, the fundamental structure resembles that of the previously produced *p*-type PQED photodiodes [1]. The Al_2O_3 layer on top of the very lightly doped silicon substrate inherently contains negative surface charge, the density of which is affected by ALD process parameters, such as temperature, surface treatment prior to ALD, and all the subsequent annealing steps. This fixed charge induces a *p*-type inversion layer in the bulk silicon, which in turn produces a depletion region. In effect, the structure generates the *pn*-junction without a diffusion process.

Two sets of photodiodes, denoted as sets A and B, were manufactured. With the exception of guard rings, the photodiode layouts of the two sets are identical. In addition to photodiodes, both sets had capacitor test structures for the

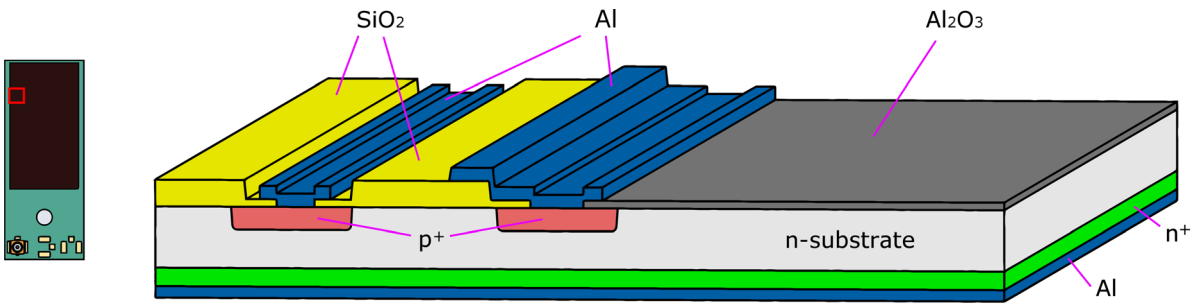

Figure 1. Cross section of the structure (not to scale) of the set B photodiode. Set A structure is identical, but instead of one guard ring (the outermost p^+ implantation) there are 16 guard rings. The red square in the left side figure of photodiode and carrier assembly indicates the cross-section area.

characterization of SiO_2 and Al_2O_3 layer properties. The area of the Al_2O_3 layer, i.e. the size of the induced junction region, is 11 mm × 22 mm. It is surrounded by ring-like p^+ diode contact and p^+ implants functioning as guard rings. Set A of photodiodes has 16 guard rings and set B has one. The back-side of the substrate is uniformly implanted with a few micrometers thick n^+ layer and metallized with a 500 nm layer of aluminium, which serves as the other diode contact. When operated, the diode is reverse biased by applying a voltage of 5–20 V between the diode contacts. This further extends the depletion region tens of micrometers into the bulk and increases the collection efficiency of charge carriers.

2.2. Photodiode processing

The *n*-type photodiodes were processed at VTT Micronova cleanroom facilities [55]. The manufacturing process is similar to that of normal *n*-type photodiodes with the addition of ALD grown Al_2O_3 layers. For starting material, two types of 150 mm-diameter double polished silicon wafers from Topsil [56] were used: a (1000 ± 20) μm thick wafer with nominal resistivity of 23 kΩ·cm for set A, and a (500 ± 10) μm thick wafer with nominal resistivity of 10 kΩ·cm for set B. The resistivities correspond to approximate phosphorous doping levels of $2 \cdot 10^{11}$ cm^{-3} and $4 \cdot 10^{11}$ cm^{-3}, respectively.

The process starts with wet oxidation at 1050 °C. The oxide layer is patterned with photolithography and used as a masking layer for the ion implantation. Screen oxide is used during implantation of boron implants on the front side and phosphorous implants on the back surface. The implanted areas are activated in an oxidation furnace at 1050 °C. After the drive-in, contact areas to the implants and induced junction area are opened to the silicon using buffered hydrofluoric acid etching. This is followed by the ALD process; 300 cycles of Al_2O_3 in a Picosun Sunale R-150B [57] ALD reactor result in the nominal layer thickness of 30 nm. After deposition, wafers are patterned, and excess Al_2O_3 is removed from areas outside induced junctions. Next the front side is metallized with aluminum and patterned, followed with back metallization and finally sintering at 425 °C.

After the processing, the photodiodes were IV-characterized for dark current density and potential breakdown behavior. As expected, the photodiodes do not suffer from breakdown problems at the low voltages used in this application. Dark current densities around 1 nA·cm^{-2} and 3 nA·cm^{-2} were measured from set A and B photodiodes, respectively.

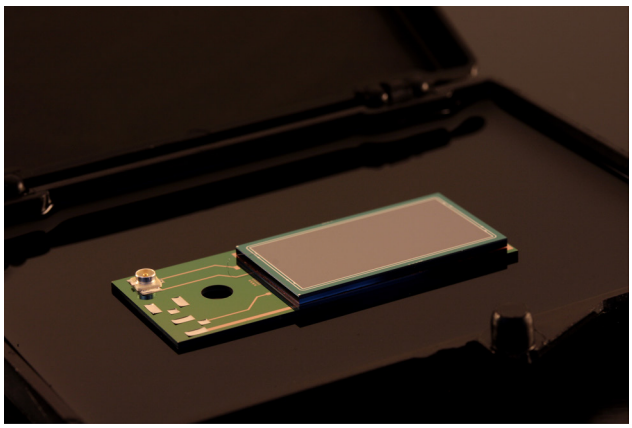

Figure 2. PQED photodiode attached to the photodiode carrier, photographed in the clean room. The assembly lays on a Gel-Pak® container, which immobilizes and protects the assembly during shipping and handling.

The final thickness of the Al_2O_3 layer is defined by the aluminum etching process, as each etching round takes away around 2–3 nm from the oxide layer. The number of etching rounds for sets A and B were one and two, resulting in nominal oxide thicknesses of 27 nm and 25 nm, respectively. In addition to processed layers, a few nanometers thick SiO_2 layer is unavoidably formed between the bulk silicon and the Al_2O_3 layer.

2.3. Photodiode carrier

The processed photodiodes were glued to carrier chips using low outgassing cryogenic glue (Stycast 8250FT/CAT9). Unlike the previous design [1], the carriers were manufactured from 1 mm thick silicon wafer. This silicon on silicon structure overcomes the problems associated with the deviating thermal expansion coefficient of the photodiode and the carrier.

For mounting purposes, a 3 mm-diameter hole is etched to the carrier chip. The photodiode signals are connected to the carrier bonding pads using aluminium wires and ultrasonic bonding, from which the signals are routed to a miniature U.FL connector on the carrier using copper metallizations. The completed photodiode and carrier assembly, shown in

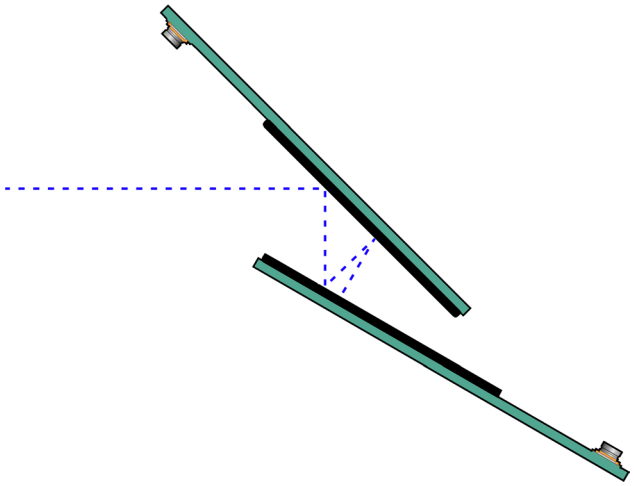

Figure 3. Schematic drawing of the light-trapping assembly. The angle between the photodiodes is 15° for the seven-reflection trap structure and 11.25° for the nine-reflection structure.

figure 2, is 15 mm × 38 mm in size, and the overall thickness with the connector is less than 3 mm.

2.4. Detector assembly

The photodiode and carrier assemblies were mounted to precision mechanics in order to achieve the wedged light-trapping configuration (see figure 3). These types of trap structures are thoroughly studied in [37, 38]. Two seven-reflection traps from both sets of photodiodes, denoted here as A1, A2, B1 and B2, were assembled and operated by Aalto University, and one nine-reflection trap from set A photodiodes, denoted as A3, was assembled and operated by Physikalisch–Technische Bundesanstalt (PTB).

In order to prevent dust and moisture contamination, the detectors were assembled in a clean room. The detectors assembled by Aalto University have air-tight cylindrical bodies with airtight caps which protect the photodiodes during storage. Unlike in the previous design of the detector [3], a Brewster window was not used in front of the trap assembly. Instead, the incident light enters photodiodes directly, similarly as in [39, 40]. When the detector is operated, dust and moisture contamination is prevented by using dry nitrogen flow through the detector frame [3]. The backside of the cylindrical detector body provides the connections for photodiode signals and nitrogen flow. The photodiodes are connected using two BNC connectors. This allows the photocurrents of both photodiodes to be measured separately. Alternatively, the photodiodes can be connected in parallel. In this case, a single current-to-voltage converter (CVC) and biasing circuitry can be used to record the total photocurrent. The BNC connectors are insulated from the detector body, enabling a floating measurement of photocurrents and a separate grounding for the housing. The PQED assembled by PTB has a cryostat housing, allowing the operation of the PQED at room and liquid nitrogen temperatures and in vacuum. A 7 mm aperture in front of the photodiodes matches the aperture in front of the receiver cavity of the cryogenic ESR of PTB, and thus

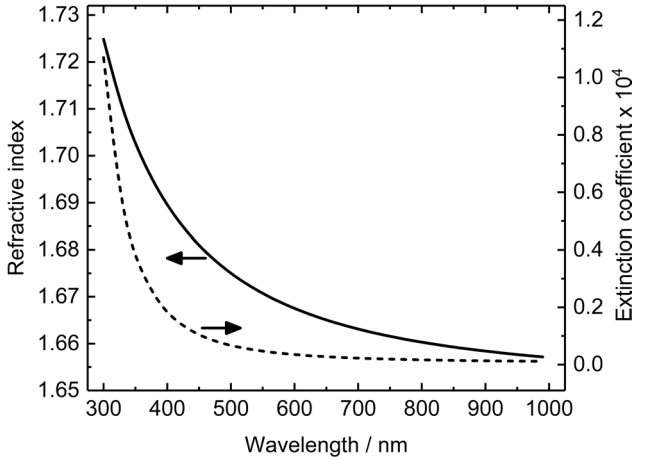

Figure 4. Refractive index and extinction coefficient of the ALD grown Al_2O_3 layer of the *n*-type PQED photodiode.

reduces the uncertainty contribution of stray radiation when PQED and cryogenic ESR are compared. This and the possibility of operating the PQED in vacuum and behind a common Brewster window enable uncertainties as low as 30 ppm in the comparison of the detectors.

The reflectance and alignment of a wedged trap detector are sensitive to the angle between the photodiodes. The angle was measured from the mechanics of the seven-reflection traps using a coordinate measuring machine. The maximum deviation from the nominal value of 15° was 0.04°, while the average deviation was 0.01°.

3. Calculated reflectance and absorption losses

3.1. Calculation method

The absorption and reflectance losses of the *n*-type PQED photodiodes were analysed using the transfer-matrix method (TMM). A comprehensive description of the method can be found in literature [58, 59]. The photodiode structure was simplified in the calculations by assuming a layer of Al_2O_3 and an interface layer of SiO_2 on infinitely thick layer of Si. This is justified, since the penetration depth of photons into silicon is in the order of micrometers at the wavelengths of interest.

By applying TMM to the layer structure of the photodiode, the specular reflectance $\rho_{r,m}(\lambda, \theta)$ and the oxide absortion $\eta_{a,m}(\lambda, \theta)$ of a single photodiode at incident angle θ and wavelength λ can be calculated. The subscript m, equal to p or s, denotes the polarization state of the incident light. The total reflection of the trap structure then becomes

$$\rho_m(\lambda) = \prod_{i=1}^{N} \rho_{r,m}(\lambda, \theta_i) \tag{3}$$

where N is the total number of reflections, 7 or 9 in this case. The incident angles are calculated as

$$\theta_i = 45° + (1 - i)\,\beta \tag{4}$$

where β is the angle between the photodiodes. Deriving the equation for total absorption losses in turn yields

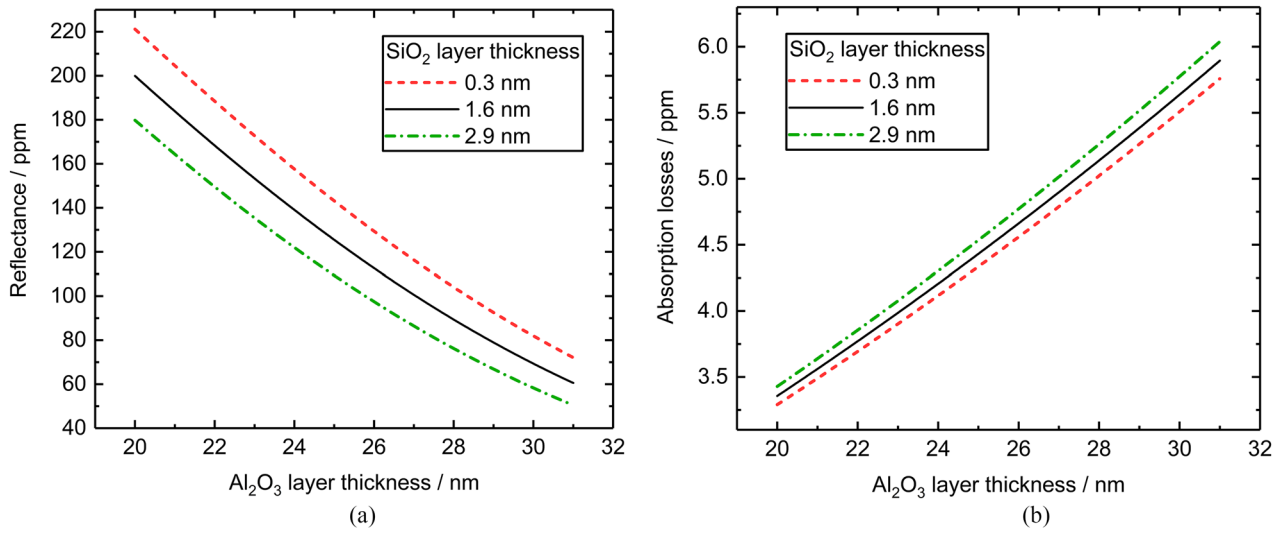

Figure 5. Calculated reflectance (a) and absorption losses (b) of the seven-reflection *n*-type PQED at the wavelength of 488 nm.

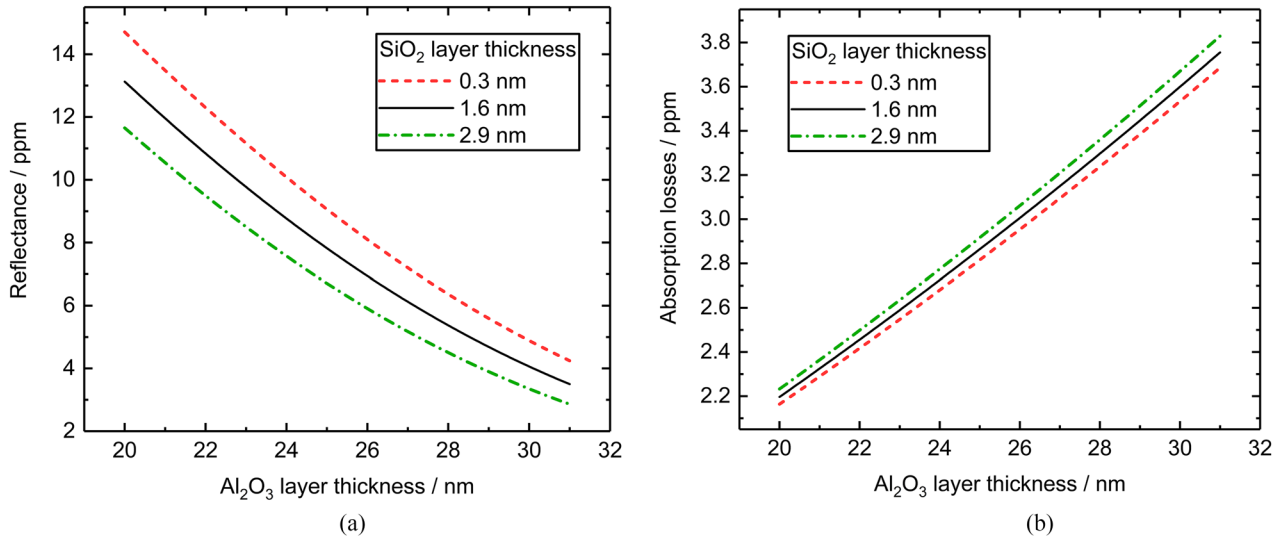

Figure 6. Calculated reflectance (a) and absorption losses (b) of the nine-reflection *n*-type PQED at the wavelength of 532 nm.

Table 1. Calculated absorption and reflectance losses of seven- and nine-reflection PQEDs assembled from set A and B photodiodes for *p* polarized light. Standard uncertainty of each value is given.

		Seven reflections		Nine reflections	
Loss	Wavelength/nm	Set A	Set B	Set A	Set B
Oxide absorption/ppm	488	4.0 ± 0.3	4.7 ± 0.4	4.1 ± 0.3	4.7 ± 0.4
	532	2.6 ± 0.2	3.0 ± 0.2	2.6 ± 0.2	3.0 ± 0.2
Reflection/ppm	488	152 ± 29	112 ± 25	13.6 ± 3.4	9.1 ± 2.7
	532	116 ± 19	89 ± 17	9.7 ± 2.0	6.9 ± 1.7

$$\eta_m(\lambda) = \eta_{a,m}(\lambda, \theta_1) + \sum_{i=2}^{N} \left[\eta_{a,m}(\lambda, \theta_i) \prod_{j=1}^{i-1} \rho_{r,m}(\lambda, \theta_j) \right]. \quad (5)$$

3.2. Calculation parameters

The required calculation parameters are the refractive indices, extinction coefficients and the layer thicknesses of the materials. The Al_2O_3 layer thicknesses were determined from two set A photodiodes and four set B photodiodes using spectroscopic ellipsometry [60, 61]. The average values obtained were (23.1 ± 1.4) nm and (26.1 ± 1.4) nm for set A and B, respectively. The quoted standard uncertainty of 1.4 nm takes into account the thickness variation across the photodiode, which has an average standard uncertainty of around 0.3 nm for the photodiodes. The SiO_2 layer thickness of the photodiodes was measured to be (1.6 ± 1.3) nm.

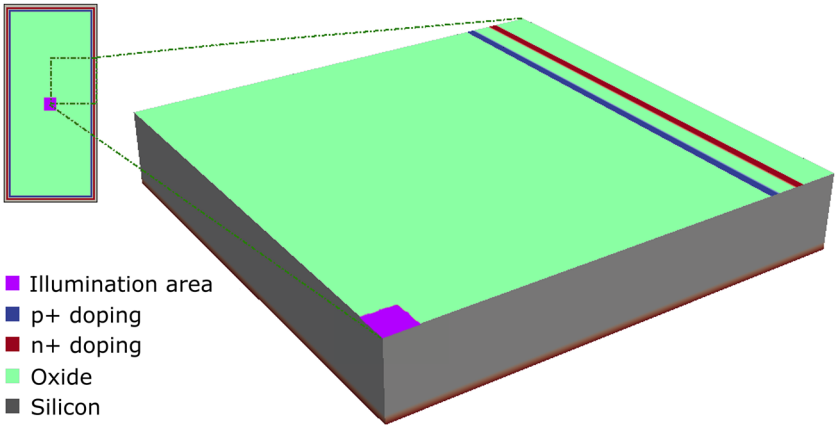

Figure 7. Simulation structure. A schematic drawing is inserted to show the simulation structure relative to the whole photodiode.

Table 2. Default modelling parameters. If the values for sets A and B deviate, the value for set B is given in parenthesis.

Parameter	Value	Reference
Bulk doping concentration/cm^{-3}	$2.5 \cdot 10^{11}$ ($4.4 \cdot 10^{11}$)	Wafer manufacturer certificate
Bulk lifetime/ms	40 (28)	Wafer manufacturer certificate
Thickness of wafer/μm	1000 (500)	Wafer manufacturer certificate
Backside doping level/cm^{-3}	10^{20}	Diode processing parameter
Photodiode size[a]/μm	6000 × 6000	Diode processing parameter
Contact ring width/μm	100	Diode processing parameter
Active area of photodiodes[a]/μm	5000 × 6000	Diode processing parameter
Power level/μW	100	
Beam size/μm	400 × 400	
Applied reverse bias voltage[b]/V	5	
Vacuum wavelength/nm	488.12	
Fixed charge density/e·cm^{-2}	$3.9 \cdot 10^{12}$ ($4.5 \cdot 10^{12}$)	See section 4.2
Surface recombination velocity/cm·s^{-1}	$3 \cdot 10^{4}$ ($5 \cdot 10^{4}$)	See section 4.2

[a] Dimensions correspond to the truncated photodiode model.
[b] When the default parameters are used, the recombination losses saturate at reverse bias voltages of 4 V or higher. Thus, the predicted IQD is valid for characterization measurements performed at 10 V bias voltage.

The refractive indices and extinction coefficients of SiO_2 and Si were interpolated from tabulated values of [61, 62], respectively. For ALD grown Al_2O_3 layers, the optical properties are dependent on the process parameters and substrate material [63, 64], and deviate significantly from that of crystalline Al_2O_3. Therefore, the complex refractive index of Al_2O_3 was measured by spectroscopic ellipsometry. The obtained values, shown in figure 4, are within the range of reported values [48, 63–65].

3.3. Calculation results

All calculations were conducted for p polarized light, as it was used in the measurements. The calculated reflectance and oxide absorption losses of a seven-reflection trap at the wavelength of 488 nm for varying Al_2O_3 and SiO_2 interface layer thicknesses are shown in figures 5(a) and (b), respectively. Similarly, the results for the nine-reflection trap at the wavelength of 532 nm are shown in figures 6(a) and (b). The wavelengths correspond to those used in the characterization of the detectors (see section 5). Although the absorption losses are dependent on the thickness of the SiO_2 layer, all absorption occurs in the Al_2O_3, as the absorption coefficient of the SiO_2 layer is identical to zero for the wavelengths of interest [61, 66].

By applying the results shown in figures 5 and 6 to layer thicknesses of set A and B photodiodes, the absorption and reflectance losses of seven- and nine-reflection PQEDs assembled from both sets were predicted for p polarized light. The values—together with estimated standard uncertainties—are given in table 1. The uncertainty analysis takes into account contributions due to layer thicknesses, photodiode alignment and complex refractive indices. Uncertainty due to photodiode alignment was estimated by varying the angle between the photodiodes (β in equation (4)) by $\pm 0.05°$.

4. Calculated recombination losses

4.1. Simulation model

As all photodiodes from the same production set are assumed to be identical with respect to charge-carrier recombination losses, the IQD is modelled for a single photodiode and applied to all photodiodes from that set. In order to predict the charge-carrier recombination losses, a 3D simulation model of the photodiode structure was built into Cogenda Genius TCAD v. 1.8.0 [53], which is a semiconductor simulation software for determining the charge carrier transport in semiconductors in

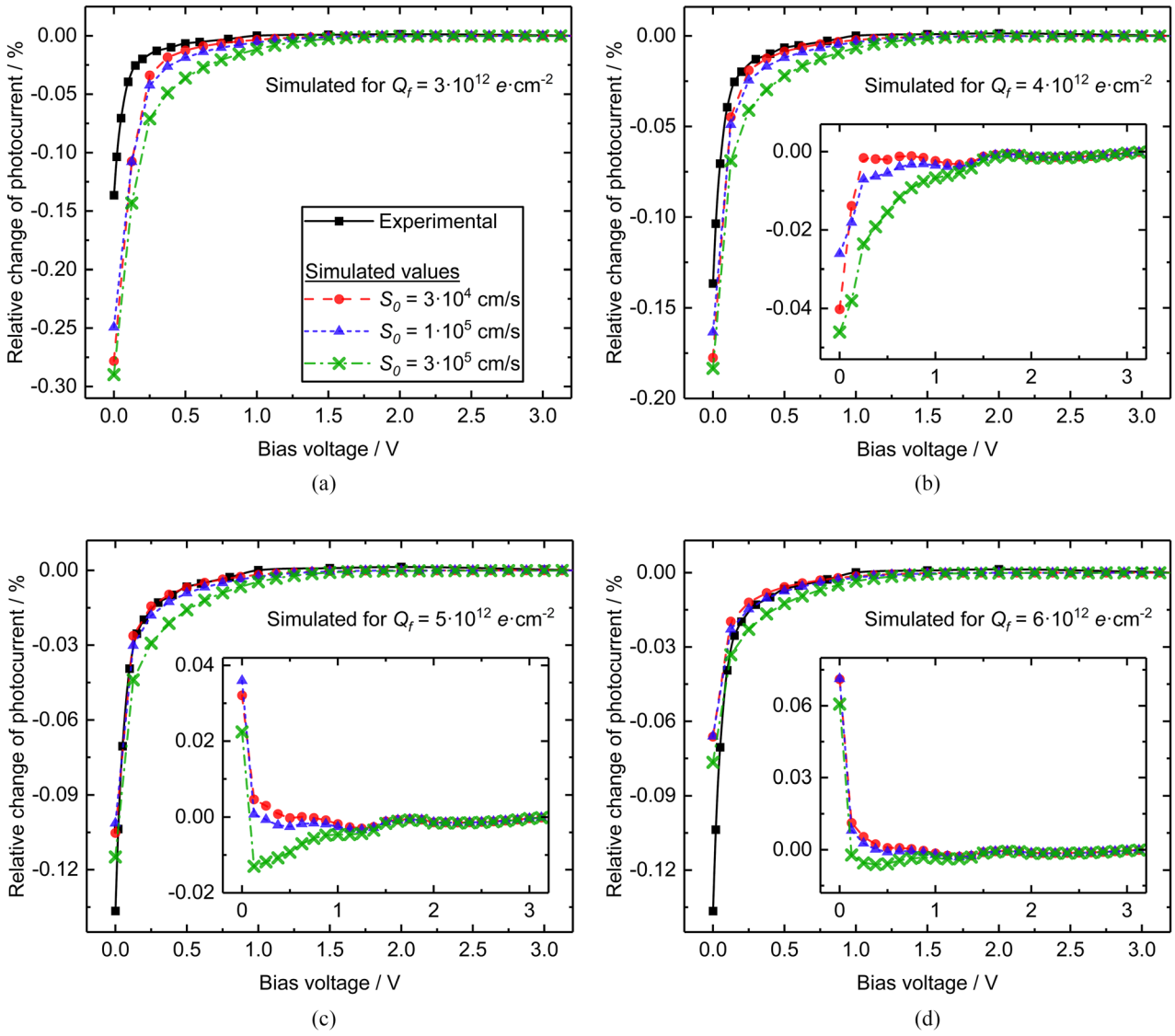

Figure 8. Measured and simulated relative change of photocurrent as a function of bias voltage for Set B photodiodes. The simulations are shown for Q_f values $3 \cdot 10^{12}$ e cm^{-2} (a), $4 \cdot 10^{12}$ e cm^{-2} (b), $5 \cdot 10^{12}$ e cm^{-2} (c) and $6 \cdot 10^{12}$ e cm^{-2} (d). The inserts show the deviations of simulated values from cubic spline interpolation of the measured values.

2D or 3D. The software solves the Poisson's equation coupled with the continuity equation of holes and electrons [67, 68]. Shockley–Read–Hall (SRH) [69, 70], direct and Auger recombination models [67, 68] are implemented by default for the bulk, and the total bulk recombination is extracted from an integral of the whole simulation device. Surface recombination rate is modelled with the equation

$$U_s = \frac{\left(n_s p_s - n_i^2\right)}{S_n^{-1}\left(n_s + n_i\right) + S_p^{-1}\left(p_s + n_i\right)}, \tag{6}$$

where n_i is the intrinsic carrier concentration, n_s and p_s are the electron and hole concentrations at the surface, respectively, and S_n and S_p are the surface recombination velocities for electrons and holes, respectively.

Equation (6) can be derived from SRH formalism. By assuming a single level defect close to the midgap, where the recombination center is most effective [68], the surface recombination rate becomes [48, 68, 71]

$$U_s = \frac{\left(n_s p_s - n_i^2\right) v_{\mathrm{th}} N_{\mathrm{it}}}{\sigma_p^{-1}\left(n_s + n_1\right) + \sigma_n^{-1}\left(p_s + p_1\right)}, \tag{7}$$

where v_{th} is the thermal velocity of the electrons, σ_p and σ_n are the hole and electron capture cross sections, respectively, N_{it} is the interface defect density and n_1 and p_1 are statistical terms. Furthermore,

$$n_1 = p_1 = n_i, \tag{8}$$

if the defect is assumed to be exactly at the middle of forbidden band [71]. Equation (6) is then obtained by denoting $S_n = v_{\mathrm{th}} N_{\mathrm{it}} \sigma_p$ and $S_p = v_{\mathrm{th}} N_{\mathrm{it}} \sigma_n$, and substituting equation (8) into (7). In our calculations, the surface recombination velocities were modelled with a single parameter for electrons and holes, $S_0 = S_n = S_p$. The parameters S_0, S_n and S_p should not be confused with the effective surface recombination velocity, S_{eff}, which is deduced from the effective lifetime of the

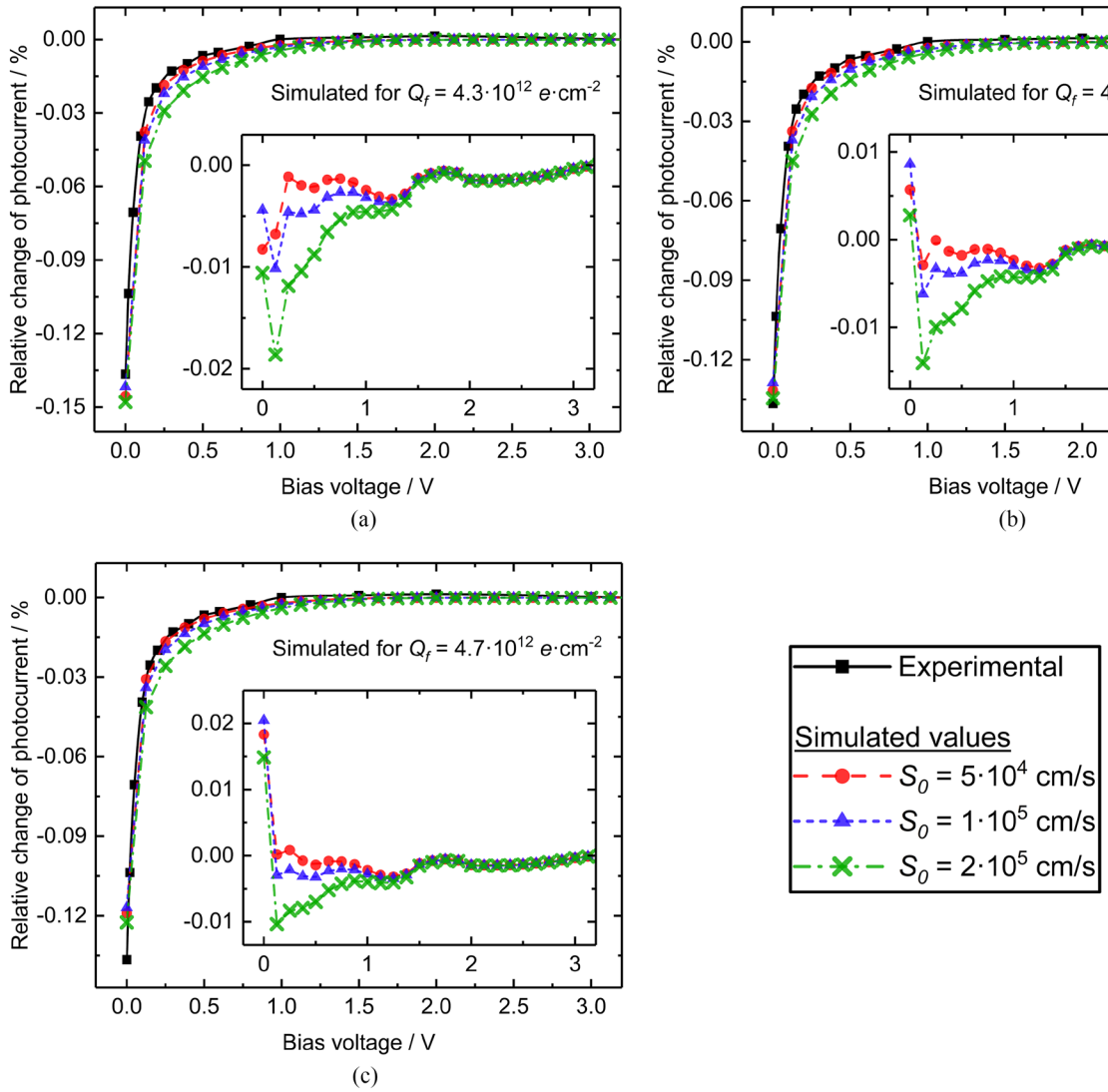

Figure 9. Measured and simulated relative change of photocurrent for Set B photodiodes. The simulations are shown for Q_f values of $4.3 \cdot 10^{12}$ e cm^{-2} (a), $4.5 \cdot 10^{12}$ e cm^{-2} (b) and $4.7 \cdot 10^{12}$ e cm^{-2} (c). The inserts show the deviations of simulated values from cubic spline interpolation of the measured values.

minority carriers in the substrate and commonly reported for photovoltaic devices [48, 72].

Figure 7 shows the simulation structure, which corresponds to 1/8 of the real device. The length truncation and symmetry are applied in order to reduce the computational requirements. Calculation is also simplified by approximating the illuminated area as a uniform square. Default input parameters for the model, given in table 2, are used in the simulations unless otherwise stated. With the exception of S_0 and Q_f, the parameters that cannot be arbitrarily selected in the manufacturing process were obtained from the wafer manufacturer or were directly measured.

4.2. Obtaining values for fixed charge density Q_f and surface recombination velocity S_0

We developed a method to extract the values for S_0 and Q_f, where the relative change of photocurrent as a function of bias voltage is measured, and the simulated bias voltage dependence of photocurrent is then fitted to the experimental data. The

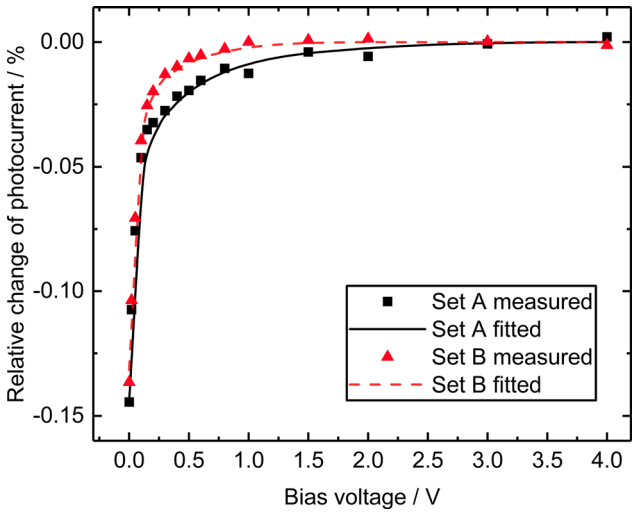

Figure 10. Measured and simulated relative change of photocurrent for both sets of photodiodes, showing the best fits. These correspond to S_0 values of $3 \cdot 10^4$ cm s^{-1} and $5 \cdot 10^4$ cm s^{-1}, and Q_f values of $3.9 \cdot 10^{12}$ e cm^{-2} and $4.5 \cdot 10^{12}$ e cm^{-2} obtained for sets A and B, respectively.

Table 3. Main uncertainty components of the calculated recombination loss at the wavelength of 488 nm. All values are given at 95% confidence level.

	Uncertainty of component		Uncertainty of recombination loss/ppm	
Component	Set A	Set B	Set A	Set B
Bulk doping concentration/cm^{-3}	$2 \cdot 10^{11}$	$2 \cdot 10^{11}$	$+30$ -7	$+20$ -7
Bulk lifetime/ms	$+10$ -25	$+10$ -15	4	6
Thickness of wafer/μm	20	40	0.1	0.1
Backside doping level/cm^{-3}	$0.2 \cdot 10^{20}$	$0.2 \cdot 10^{20}$	0.1	0.1
Length and width of the active area[a]/μm	20	20	0.01	0.01
Beam intensity profile			0.1	0.1
FC density/e·cm^{-2}	$0.2 \cdot 10^{12}$	$0.2 \cdot 10^{12}$	6	6
SRV/cm·s^{-1}	$+1.5 \cdot 10^{5}$ $-2 \cdot 10^{4}$	$+1.5 \cdot 10^{5}$ $-2 \cdot 10^{4}$	$+67$ -9	$+64$ -8
Combined uncertainty			$+74$ -13	$+68$ -14

[a] Includes the component arising from the truncated photodiode model.

measurement is straightforward; a single photodiode or a trap assembly is illuminated with stabilized laser beam. In the latter case, only the photocurrent of one of the photodiodes is taken into analysis and the other can be used as a monitor detector signal, as was done here. A rough estimate of the optical power absorbed by the photodiode needs to be known. Easiest way to determine this is to assume the photodiode to be ideal, as the IQD of the PQED is insignificantly small compared to the required accuracy of around 5%. Optionally, the incident power can be measured with another calibrated detector.

Fitting parameters S_0 and Q_f to experimental values is essentially a task of nonlinear numerical optimization. Various algorithms, such as the Nelder–Mead method [73], can be applied to such problems. However, since the computational time required for the calculation of one curve, i.e. the bias voltage dependency of the responsivity with a single combination of the two parameters, is around 1 h, the time required to find an ideal fit becomes exceedingly long. Therefore, a systematic manual approach described below was used. Examples are shown for set B, but identical treatment was made for set A also. It should be noted, that Q_f can also be determined using contactless capacitance–voltage measurement [74, 75]. The Q_f was measured from test structures on the wafers using this method. However, the accuracy was found to be insufficient, as each measurement affects the observed charge and the reproducibility of the measurement is poor. Nonetheless, the method can still be useful, as it provides a rough estimate of Q_f to facilitate the curve fitting. In this case, it was estimated that for both sets the Q_f values are in the range of $2 \cdot 10^{12}$ e cm^{-2} to $7 \cdot 10^{12}$ e cm^{-2}.

For both sets, the modelled relative change of photocurrent as a function of bias voltage was modelled for Q_f values ranging from $2 \cdot 10^{12}$ e cm^{-2} to $6 \cdot 10^{12}$ e cm^{-2} and S_0 values ranging from $1 \cdot 10^{4}$ cm s^{-1} to $3 \cdot 10^{5}$ cm s^{-1}. The IQD saturates when the reverse bias voltages is around 4 V or higher and the relative change is given as relative deviation from the saturated value. The studied characteristics of the curves are the relative deviation of the zero bias photocurrent from saturated value, referred to as the amplitude of the curve, and the shape of the curve.

Figures 8(a)–(d) show, together with the experimental values, the modelled relative change of photocurrent for set B photodiodes for Q_f values from $3 \cdot 10^{12}$ e cm^{-2} to $6 \cdot 10^{12}$ e cm^{-2} and S_0 values from $3 \cdot 10^{4}$ cm s^{-1} to $3 \cdot 10^{5}$ cm s^{-1}. Extreme boundaries of the Q_f are easy to determine; either the amplitude or the shape of the curve—or both—differ significantly from the measured curve regardless of the S_0 value. At Q_f values of $4 \cdot 10^{12}$ e cm^{-2} and $5 \cdot 10^{12}$ e cm^{-2}, the S_0 value of around $1 \cdot 10^{5}$ cm s^{-1} gives the smallest amplitude; increasing or decreasing S_0 increases the amplitude, which also makes the match to the experimental amplitude worse in all cases. With additional calculations, the S_0 and Q_f values can be further iterated. Interpolated curve at $Q_f = 4.5 \cdot 10^{12}$ e cm^{-2} and $S_0 = 1 \cdot 10^{5}$ cm s^{-1} gave a reasonable fit. This point served as the initial guess for the next round of calculations, shown in figures 9(a)–(c), where Q_f values range from $4.3 \cdot 10^{12}$ e cm^{-2} to $4.7 \cdot 10^{12}$ e cm^{-2} and S_0 values from $5 \cdot 10^{4}$ cm s^{-1} to $2 \cdot 10^{5}$ cm s^{-1}. The best fits for both sets are shown in figure 10.

4.3. Simulation results

Using the parameters given in table 2, the calculated recombination losses at the wavelength of 488 nm for sets A and B become 14^{+74}_{-13} ppm and 21^{+68}_{-14} ppm, respectively. The quoted 95% confidence interval was estimated by varying the parameters within reasonable limits and by testing the effects of the assumptions related to calculations. The uncertainty budget is given in table 3.

The largest contributions to the uncertainty of the calculated recombination losses come from the uncertainty of bulk doping concentration and the parameters S_0 and Q_f. In the experimental results, the standard uncertainty of the relative change of photocurrent is around 0.01% and 0.003% for sets A and B, respectively, and it is dominated by the random

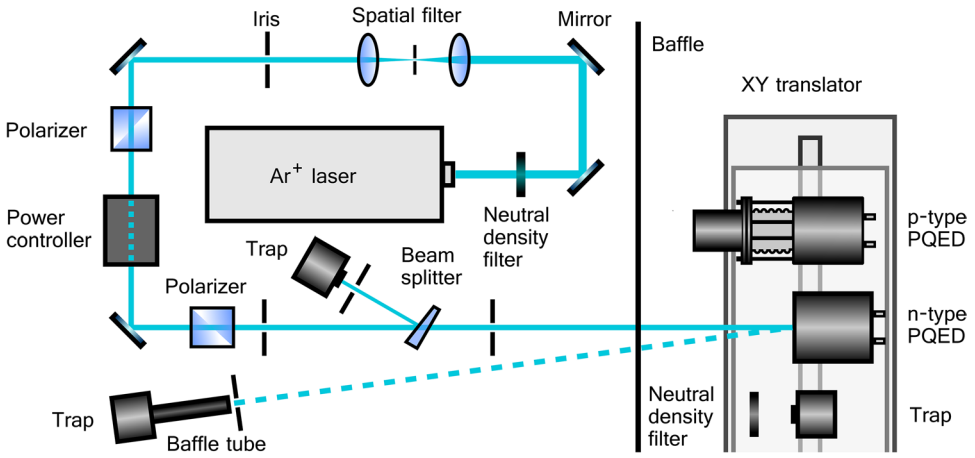

Figure 11. Block diagram of the measurement setup at Aalto University. The detectors are nominally aligned so that the backreflection of the beam from the detector is parallel with the incident beam. For reflectance measurement (dashed beam) the detector under test was rotated 1.5°. The trap detector behind the neutral density filter was used for linearity measurements.

Table 4. Measurement parameters in the characterization measurements at Aalto University and at PTB.

	Aalto University	PTB
Vacuum wavelength/nm	488.12	532
Optical power/μW	100	240
Beam diameter (e^{-2})/mm	1.0	3.4
Polarization	*p*	*p*
PQED bias voltage/V	10	5
Number of reflections in PQED	7	9

component. The bias voltage was measured with a multimeter connected in parallel with the photodiode. This measurement had an absolute standard uncertainty of around 30 μV, calibration uncertainty of the multimeter being the largest uncertainty component. The thermoelectric effects were assumed to be negligible, since the Seebeck coefficients of common cable and connector materials are around ±2 μV·K^{-1} [76] and the temperature gradients in the controlled laboratory environment are less than 1 K. At the steepest point, the relative change of photocurrent has a slope of about 1.7%·V^{-1}. Thus, in terms of relative change of photocurrent, the uncertainty due to bias voltage measurement is insignificant.

The uncertainty due to bulk lifetime and doping concentration was estimated by varying parameters one at a time within the 95% confidence interval and performing the fitting process of section 4.2. Reducing the bulk lifetime leads into increased Q_f and decreased S_0, and vice versa. Changing the doping concentration has little effect on the amplitude of the curve, but the shape of the curve needs to be altered by changing the S_0 value.

5. Characterization measurements

Characterization measurements were performed at Aalto University using power stabilized Ar$^+$ laser operated at the vacuum wavelength of 488.12 nm. The guard rings of the photodiodes were left floating in all measurements. Seven-reflection PQEDs assembled from both sets of photodiodes were characterized for spatial uniformity of responsivity and photocurrent ratio, specular reflectance, and absolute

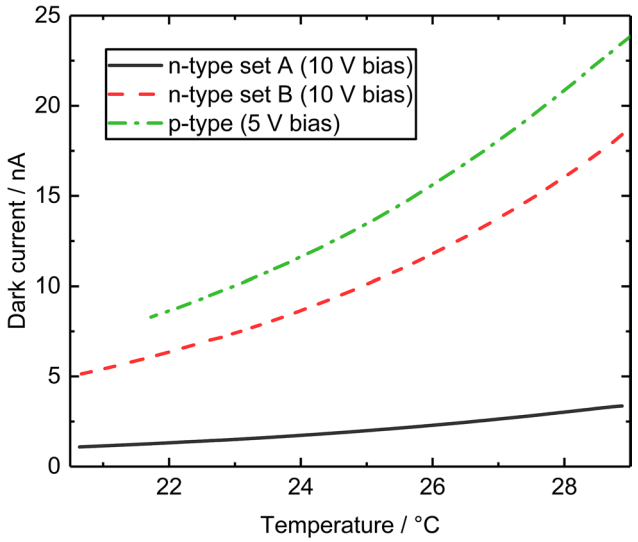

Figure 12. Temperature dependence of dark current for *n*-type photodiodes of both sets and for a *p*-type photodiode similar to that characterized in [1–3]. The *p*-type photodiode was reverse biased to 5 V, whereas nominal 10 V bias was used for *n*-type photodiodes.

responsivity. In addition, the linearity of a PQED from set A and temperature dependence of dark current for a photodiode from both sets were measured. With the exception of the latter, all measurements were performed at room temperature. A schematic of the setup used for characterization measurements is shown in figure 11. For all measurements, unless otherwise specified, the detector was aligned in such a way that the beam hits the centre of the active area of the detector. This was achieved by moving the PQED in front of the laser beam using an *xy* translator and finding the edges of the active area. The centre of the active area is then taken as the midpoint of the edge-to-edge distances along horizontal and vertical axes.

In addition to characterization measurements by Aalto University, the absolute responsivity of a nine-reflection PQED assembled from set A photodiodes was measured at the wavelength of 532 nm by PTB at room temperature. Further details of measurement conditions are given in table 4.

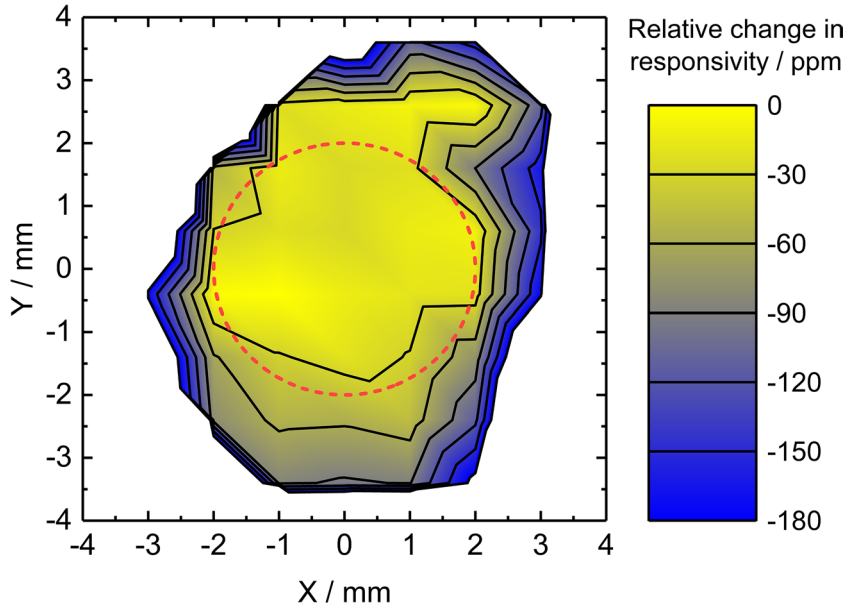

Figure 13. Spatial uniformity of responsivity for the PQED labelled as A1. Values are given as a relative deviation from the measured peak value. Reduced responsivity at the sides may be caused by loss of weak scattered radiation outside the main beam. A 4-mm-diameter circle with uniform responsivity is shown by the dashed red line.

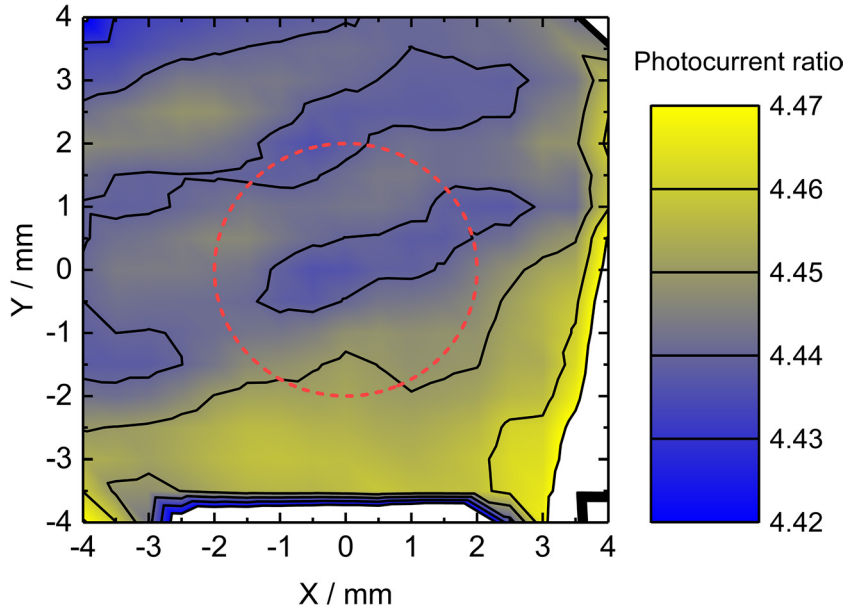

Figure 14. Spatial variation in the photocurrent ratio of the PQED labelled as A1. The dashed red line corresponds to that of figure 13.

5.1. Temperature dependence of dark current

The temperature dependence of dark current, shown in figure 12, was measured from a single photodiode of both sets. The photodiodes were heated in the thermally isolated container and then left to cool down slowly to a near steady state temperature over a period of 24 h, while constantly monitoring temperature and dark current. For comparison, an earlier measurement of a *p*-type PQED dark current at 5 V bias voltage is also shown. Both the dark current and its temperature dependence are significantly lower in the set A photodiode even though it is made using substrate twice as thick as that of set B. This is probably due to higher resistivity of the substrate and larger number of guard rings in the set A photodiode layout. These dark current properties become significant when low flux levels are measured, for example, in photometric applications [39, 40] or single photon applications [34].

5.2. Spatial uniformity of responsivity

The spatial uniformity of the responsivity was measured with a two-axis linear translator. The active area was scanned in both directions with 1 mm steps from −4 to +4 mm relative to the centre of the active area. The results, presented for the PQED labelled as A1 in figure 13, indicate that with a laser beam diameter of 1 mm, the responsivity changes less than 30 ppm within a diameter of approximately 4 mm around the

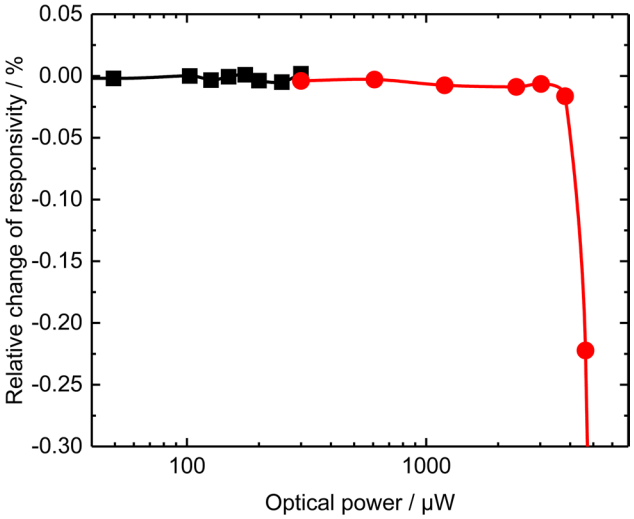

Figure 15. Relative change of responsivity as a function of incident flux, measured from the PQED labelled A1. Higher power levels were measured with a neutral density filter in front of the reference detector (red dots). The solid line is a guide to eye.

signal centre in all detectors; similar uniformity was measured also for set B detectors. Thus, the spatial uniformity of the *n*-type PQED can match that of the *p*-type PQEDs [3].

5.3. Spatial uniformity of photocurrent ratio

Figure 14 shows the photocurrent ratio of the two *n*-type photodiodes of the detector A1. The measured values across the detector are in agreement with the modelled value of 4.52 ± 0.16 ($k = 2$). Similarly to the *p*-type PQEDs, the photocurrent ratio of the *n*-type PQEDs shows a peak-to-peak variation of about 1% over the active area. It is remarkable that a feature of this magnitude is not seen in the spatial uniformity of the detectors. In addition to oxide thickness variations of the photodiodes, the non-uniformity in figure 13 is affected by non-uniform IQD, point-like defects on the surface of the photodiodes (e.g. dust particles), the entrance aperture shadowing the beam at large distances from the detector centre, and measurement noise. Consequently, the IQD of the *n*-type photodiodes is concluded to be spatially uniform at least within 30 ppm and the spatial variation of the photocurrent ratio is mainly due to variations in the photodiode reflectance.

5.4. Linearity

Figure 15 shows the linearity of the detector A1, which was measured by adjusting the optical power with neutral density filters in front of the laser and with the liquid crystal based power stabilizer (see figure 11). A three-element reflectance trap built from Hamamatsu S1337 photodiodes was used as a reference. The responsivity of the Hamamatsu S1337 has been demonstrated to be linear up to photocurrents of 100 µA [77–80]. At higher power levels, a neutral density filter was used in front of the reference detector to maintain operation at the linear range. The non-linearity of the PQED, albeit measured with both photodiodes in parallel, is most probably dominated

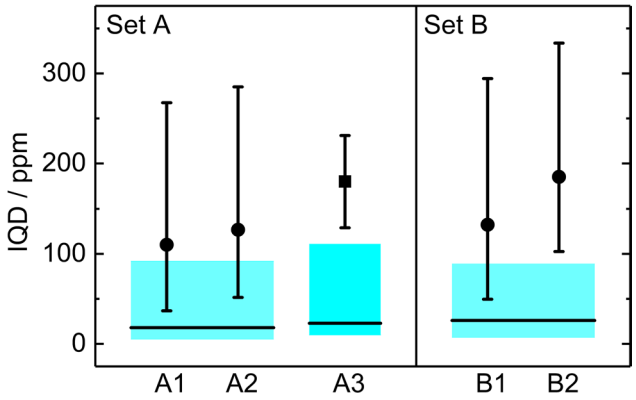

Figure 16. Absolute IQD measured at 488 nm (dots) and 532 nm (square). Black horizontal lines show the predicted IQD and cyan boxes indicate the estimated uncertainty of the model. Uncertainties are given at 95% confidence level.

by the saturation of the first photodiode, as it measures about 80% of the incident flux at 488 nm.

5.5. Specular reflectance

The dashed line in figure 11 shows the measurement scheme for specular reflectance. The power of the incident laser beam was measured with the PQED under test and a conventional three-element reflection trap detector was used to collect the reflected light from the PQED. This trap was compared against one of the PQEDs to determine its responsivity. The uncertainty budget of the reflectance measurement is similar to that given in [3], with the exception of components arising from the Brewster window, which in this case can be omitted. Typical absolute standard uncertainty of measured reflectance is around 0.2 ppm, where the largest component of uncertainty is the reproducibility of the measurements.

The measured values of reflectance at the wavelength of 488 nm were (172.8 ± 0.2) ppm and (155.5 ± 0.2) ppm for detectors A1 and A2, respectively. For set B, the deviation was smaller; the measured reflectances were (109.3 ± 0.2) ppm for B1 and (111.3 ± 0.2) ppm for B2. All measurement results are well within the standard uncertainty of the modelled reflectance.

5.6. Absolute responsivity

P-type PQEDs, similar to those characterized in [1–3], were used as references in the absolute responsivity measurements of the *n*-type PQEDs. The reference at PTB was compared against cryogenic ESR, whereas the responsivity of the reference at Aalto University and its uncertainty were predicted according to [1, 33]. The IQD value of PQED A3 was determined by correcting the measured responsivity with the calculated reflectance of (9.7 ± 2.0) ppm (see table 1). For others, the measured reflectance values were used. The measured IQD values together with the predicted values are shown in figure 16. The predicted value is calculated as the sum of absorption and recombination losses, while the combined uncertainty is taken as a quadrature sum of the uncertainties

(see tables 1 and 3). The effect of quantum gain is in the order of 10^{-8} [33] and is neglected.

6. Conclusions

The first ever PQED to utilize *n*-type silicon and Al_2O_3 layer to form the induced junction was developed, manufactured, modelled and characterized. Due to the high fixed charge density, the Al_2O_3 layer can be a factor of 10 thinner than the SiO_2 layers used with *p*-type PQED photodiodes. Two sets of detectors with different substrate doping concentrations and thicknesses were manufactured. ALD was used to grow the Al_2O_3 layer, as it provides a controlled method to produce uniform oxide layers to an atomically specified thickness.

The absorption and reflectance losses of the *n*-type PQED photodiodes were analysed using the TMM. For the calculations, the thickness and complex refractive index of the ALD grown Al_2O_3 layer were measured by spectroscopic ellipsometry. The reflectance and absorption losses both show a monotonic behaviour as a function of Al_2O_3 layer thickness. This suggests that the spatial variation of photocurrent ratio or reflectance could possibly be used to estimate the uniformity in the thickness of the oxide layer. Future work could include further investigation of these possibilities similarly as was done in [3, 38] for the *p*-type PQED.

In order to predict recombination losses, a 3D simulation model of the photodiode structure was built into Cogenda Genius semiconductor simulation software. The input parameters in the simulation are either obtained from wafer manufacturer, selected in the manufacturing processing, or they can be directly measured. A novel method to extract the values for the fixed charge density and the surface recombination velocity of electrons and holes was developed, where the relative change of photocurrent as a function of bias voltage is measured, and the simulated bias voltage dependence of photocurrent is then fitted to the experimental data. This makes the prediction of the PQED responsivity a completely autonomous process.

The characterization measurements at the wavelength of 488 nm showed beneficial features for *n*-type photodiodes as compared with the earlier *p*-type PQED photodiodes. For both sets of photodiodes, the responsivity of the assembled PQEDs is uniform within 30 ppm in the central area of 4 mm in diameter. Set A photodiodes were measured to be linear up to about 4 mW of radiant flux with reverse bias voltage of 10 V. This result is also consistent with the calculated linearity. For comparison, the *p*-type photodiodes are measured to be linear up to 400 μW at the wavelength of 760 nm and with 5 V bias [2]. In addition, the dark current of the set A photodiodes, and its temperature dependence, were shown to be significantly smaller than those of *p*-type PQEDs. This property is favorable when radiant flux in the few photon regime is measured. Such a detector based on a single PQED photodiode is in development.

The predicted and measured responsivities of the *n*-type PQEDs show a systematic underestimation of the predicted IQD at the wavelengths of 488 nm and 532 nm. Possible explanations are the limitations and simplifications of the 1D model used to predict the spectral responsivity of the *p*-type PQEDs which has been used as reference in the determination of the IQD of *n*-type PQEDs at the wavelength of 488 nm. However, the IQD of PQED A3 at the wavelength of 532 nm measured against a cryogenic radiometer is significantly larger than the predicted IQD, too. This indicates that also the 3D model might underestimate the IQD. A reason for the higher than expected quantum deficiencies could be residual contaminations on the photodiode surface, and simplifications and limitations of the 3D model. Further investigation of the method to obtain simulation parameters is also needed. For example, the bias voltage dependence of the responsivity could be measured at different wavelengths and power levels.

The results obtained in this research indicate that the *n*-type induced junction photodiode is a very promising alternative to the existing *p*-type detectors. Consequently, it proves that the manufacturing of PQEDs is no longer dependent on the availability of a particular silicon process. Finally, it gives additional credibility to the concept of a modelled quantum detector serving as a primary standard.

Acknowledgments

The authors are grateful to WMM Kessels for discussions. The research leading to these results has received funding from the European Metrology Research Programme (EMRP) project SIB57 'New Primary Standards and Traceability for Radiometry'. The EMRP is jointly funded by the EMRP participating countries within EURAMET and the European Union. Financial support from the Academy of Finland through the Finnish Centre of Excellence in Atomic Layer Deposition is also acknowledged.

ORCID iDs

Timo Dönsberg https://orcid.org/0000-0002-7783-4244

References

[1] Sildoja M, Manoocheri F, Merimaa M, Ikonen E, Müller I, Werner L, Gran J, Kübarsepp T, Smid M and Rastello M L 2013 Predictable quantum efficient detector: I. Photodiodes and predicted responsivity *Metrologia* **50** 385–94

[2] Müller I *et al* 2013 Predictable quantum efficient detector: II. Characterization and confirmed responsivity *Metrologia* **50** 395–401

[3] Dönsberg T, Sildoja M, Manoocheri F, Merimaa M, Petroff L and Ikonen E 2014 A primary standard of optical power based on induced-junction silicon photodiodes operated at room temperature *Metrologia* **51** 197–202

[4] 2015 SI brochure appendix 2. *Mise en pratique* for the definition of the candela and associated derived units (BIPM) available at www.bipm.org/utils/en/pdf/SIApp2_cd_en.pdf

[5] Datla R U and Parr A C 2005 Introduction to optical radiometry *Optical Radiometry* ed A C Parr *et al* (Amsterdam: Elsevier)

[6] Fox N P 2000 Primary radiometric quantities and units *Metrologia* **37** 507–13

[7] Zwinkels J C, Ikonen E, Fox N P, Ulm G and Rastello M L 2010 Photometry, radiometry an 'the candela': evolution in the classical and quantum world *Metrologia* **47** R15–32

[8] Friedrich R and Fischer J 2000 New spectral radiance scale from 220 nm to 2500 nm *Metrologia* **37** 539–42

[9] Arp U, Friedman R, Furst M L, Makar S and Shaw P S 2000 SURF III—an improved storage ring for radiometry *Metrologia* **37** 357–60

[10] Klein R, Brandt G, Fliegauf R, Hoehl A, Müller R, Thornagel R and Ulm G 2009 The metrology light source operated as a primary source standard *Metrologia* **46** S266–71

[11] Beckhoff B, Gottwald A, Klein R, Krumrey M, Müller R, Richter M, Scholze F, Thornagel R and Ulm G 2009 A quarter-century of metrology using synchrotron radiation by PTB in Berlin *Phys. Status Solidi* b **246** 1415–34

[12] Polyakov S V and Migdall A L 2007 High accuracy verification of a correlated-photon-based method for determining photon-counting detection efficiency *Opt. Express* **15** 1390–407

[13] Chunnilall C J, Degiovanni I P, Kück S, Müller I and Sinclair A G 2014 Metrology of single-photon sources and detectors: a review *Opt. Eng.* **53** 081910

[14] Martin J E, Fox N P and Key P J 1985 A cryogenic radiometer for absolute radiometric measurements *Metrologia* **21** 147–55

[15] Varpula T, Seppä H and Saari J M 1989 Optical power calibrator based on a stabilized green He–Ne laser and a cryogenic absolute radiometer *IEEE Trans. Instrum. Meas.* **38** 558–64

[16] Fox N P and Rice J P 2005 Absolute radiometers *Optical Radiometry* ed A Parr *et al* (Amsterdam: Elsevier)

[17] Gentile T R, Houston J M, Hardis J E, Cromer C L and Parr A C 1996 High accuracy cryogenic radiometer *Appl. Opt.* **35** 1056–68

[18] Werner L and Hartmann J 2009 Calibration and interpolation of the spectral responsivity of silicon photodiode-based detectors *Sens. Actuators* A **156** 185–90

[19] Goebel R, Stock M and Köhler R 2000 Report on the international comparison of cryogenic radiometers based on transfer detectors *Bureau International Des Poids et Mesures Report*-2000/9 available at www.bipm.org/pdf/RapportBIPM/2000/09.pdf

[20] Goebel R and Stock M 2004 Report on the key comparison CCPR-K2.b of spectral responsivity measurements in the wavelength range 300 nm to 1000 nm available at www.bipm.org/utils/common/pdf/final_reports/PR/K2/CCPR-K2.b.pdf

[21] Brown S W, Larason T C and Ohno Y 2009 Report on the key comparison CCPR-K2.a-2003 spectral responsivity in the range of 900 nm to 1600 nm available at http://kcdb.bipm.fr/AppendixB/appbresults/ccpr-k2.a/ccpr-k2.a_final_report.pdf

[22] Geist J 1979 Quantum efficiency of the *p-n* junction in silicon as an absolute radiometric standard *Appl. Opt.* **18** 760–2

[23] Zalewski E F and Geist J 1980 Silicon photodiode absolute spectral response self-calibration *Appl. Opt.* **19** 1214–6

[24] Geist J, Zalewski E F and Schaefer A R 1980 Spectral response self-calibration and interpolation of silicon photodiodes *Appl. Opt.* **22** 3795–9

[25] Geist J, Liang E and Schaefer A R 1981 Complete collection of minority carriers from the inversion layer in induced junction diodes *J. Appl. Phys.* **52** 4879–81

[26] Zalewski E F and Duda C R 1983 Silicon photodiode device with 100% external quantum efficiency *Appl. Opt.* **22** 2867–73

[27] Booker R L and Geist J 1984 Induced junction (inversion layer) photodiode self-calibration *Appl. Opt.* **23** 1940–5

[28] Geist J and Baltes H 1989 High accuracy modeling of photodiode quantum efficiency *Appl. Opt.* **28** 3929–39

[29] Geist J, Brida G and Rastello M L 2003 Prospects for improving the accuracy of silicon photodiode self-calibration with custom cryogenic photodiodes *Metrologia* **40** S132–5

[30] Gran J 2005 Accurate and independent spectral response scale based on silicon trap detectors and spectrally invariant detectors *Dissertation for the Degree of Doctor Scientarium* University of Oslo

[31] Gran J and Tang C K 2017 Validation that Hamamatsu 1337 trap detectors are independently predictable when using a hybrid self-calibration method *Proc. NEWRAD 2017 Conf. (Tokyo, Japan)* pp 168–9

[32] Gran J and Sudbø A S 2004 Absolute calibration of silicon photodiodes by purely relative measurements *Metrologia* **41** 204–12

[33] Gran J, Kübarsepp T, Sildoja M, Manoocheri F, Ikonen E and Müller I 2012 Simulations of a predictable quantum efficient detector with PC1D *Metrologia* **49** S130–4

[34] Manoocheri F, Sildoja M, Dönsberg T, Merimaa M and Ikonen E 2014 Low-loss photon-to-electron conversion *Opt. Rev.* **21** 320–4

[35] Hansen T 1978 Silicon UV-photodiodes using natural inversion layers *Phys. Scr.* **18** 471–5

[36] Tang C K, Gran J, Müller I, Linke U and Werner L 2015 Measured and 3D modelled quantum efficiency of an oxide-charge induced junction photodiode at room temperature *15th Int. Conf. on Numerical Simulation of Optoelectronic Devices (Taipei, Taiwan)* pp 177–8 available at www.nusod.org/2015/nusod15_paper89.pdf

[37] Sildoja M, Manoocheri F and Ikonen E 2009 Reflectance calculations for a predictable quantum efficient detector *Metrologia* **46** S151–4

[38] Sildoja M, Dönsberg T, Mäntynen H, Merimaa M, Manoocheri F and Ikonen E 2014 Use of the predictable quantum efficient detector with light sources of uncontrolled state of polarization *Meas. Sci. Technol.* **25** 015203

[39] Dönsberg T, Pulli T, Poikonen T, Baumgartner H, Vaskuri A, Sildoja M, Manoocheri F, Kärhä P and Ikonen E 2014 New source and detector technology for the realization of photometric units *Metrologia* **51** S276–81

[40] Pulli T, Dönsberg T, Poikonen T, Manoocheri F, Kärhä P and Ikonen E 2015 Advantages of white LED lamps and new detector technology in photometry *Light Sci. Appl.* **4** e332

[41] Kübarsepp T, Pokatilov A, Kruusla H, Dhoska K, Brida G, Gran J, Tang C K, Dönsberg T, Manoocheri F and Ikonen E 2017 PQED for measurement of fiber optic power *Proc. NEWRAD 2017 Conf. (Tokyo, Japan)* pp 120–1

[42] Rougié B, Coutin J M and Renoux D 2015 Un nouvel étalon de référence pour la sensibilité spectrale de détecteur, 'peu couteux' et de très faible incertitude *Proc. of 17th Int. Congress of Metrology (Paris, France)* p 11002 available at http://cfmetrologie.edpsciences.org/articles/metrology/pdf/2015/01/metrology_metr2015_11002.pdf

[43] White M, Gran J, Tomlin N and Lehman J 2014 A detector combining quantum and thermal primary radiometric standards in the same artefact *Metrologia* **51** S245–51

[44] Borroguero E, Tang C K, Gran J, Pons A, Campos J, Hernarz M L, Velázquez J L and Bernad B 2015 Self-calibration of silicon photodiodes internal quantum efficiency by using temperature sensors *Resúmenes de las contribuciones a la XI Reunión Nacional de Óptica (Salamanca, Spain)* p 149 available at https://digital.csic.es/handle/10261/134878

[45] Nordsveen M U, Tang C K and Gran J 2017 Demonstration of a dual-mode Si detector as a self-calibrating device at room temperature *Opt. Express* **25** 8459–69
[46] Nordsveen M U, Tang C K and Gran J 2017 The self-calibrating dual-mode Si detector—improved design based on comsol multiphysics simulations *Conf. on Lasers and Electro-Optics 2017 (San Jose, California, USA)* paper ATh3B.7 (https://doi.org/10.1364/CLEO_AT.2017.ATh3B.7)
[47] Deal B E, Sklar M, Grove A S and Snow E H 1967 Characteristics of the surface-state charge (Q_{ss}) of thermally oxidized silicon *J. Electrochem. Soc.* **114** 266–74
[48] Dingemans G and Kessels W M 2012 Status and prospects of Al_2O_3-based surface passivation schemes for silicon solar cells *J. Vac. Sci. Technol.* A **30** 040802
[49] Leskelä M and Ritala M 2002 Atomic layer deposition (ALD): from precursors to thin film structures *Thin Solid Films* **409** 138–46
[50] George S 2010 Atomic layer deposition: an overview *Chem. Rev.* **110** 111–31
[51] Valluru D 2015 Surface passivated black silicon photodetectors with induced junction *Master's Theses* Aalto University
[52] Juntunen M A, Heinonen J, Vähänissi V, Repo P, Valluru D and Savin H 2016 Near-unity quantum efficiency of broadband black silicon photodiodes with an induced junction *Nat. Photon.* **10** 777–81
[53] Cogenda Pte Ltd 2016 Genius semiconductor device simulator V1.8.0 manual available at www.cogenda.com/article/downloads
[54] Hoem S, Gran J, Sildoja M, Manoocheri F, Ikonen E and Müller I 2011 Physics of self-induced photodiodes *Proc. NEWRAD 2011 Conf. (Maui, Hawaii, USA)* pp 259–60 available at http://newrad2011.aalto.fi
[55] www.micronova.fi
[56] www.topsil.com
[57] www.picosun.com
[58] Macleod H A 2010 *Thin-Film Optical Filters* (Boca Raton, FL: CRC Press)
[59] Yeh P 2005 *Optical Waves in Layered Media* (New York: Wiley-Interscience)
[60] Tompkins H G and Irene E A 2005 *Handbook of Ellipsometry* (Norwich: William Andrew)
[61] White M, Lolli L, Brida G, Gran J and Rajteri M 2013 Optical constants and spatial uniformity of thermally grown oxide layer of custom, induced-junction, silicon photodiodes for a predictable quantum efficient detector *J. Appl. Phys.* **113** 243509
[62] Green M A 2008 Self-consistent optical parameters of intrinsic silicon at 300K including temperature coefficients *Sol. Energy Mater. Sol. Cells* **92** 1305–10
[63] Aguilar-Gama M T, Ramírez-Morales E, Montiel-González Z, Mendoza-Galván A, Sotelo-Lerma M, Nair P K and Hu H 2015 Structure and refractive index of thin alumina films grown by atomic layer deposition *J. Mater. Sci., Mater. Electron.* **26** 5546–52
[64] Kim Y, Lee S M, Park C S, Lee S I and Lee M Y 1997 Substrate dependence on the optical properties of Al_2O_3 films grown by atomic layer deposition *Appl. Phys. Lett.* **71** 3604–6
[65] Aslan M M, Webster N A, Byard C L, Pereira M B, Hayes C M, Wiederkehr R S and Mendes S B 2010 Low-loss optical waveguides for the near ultra-violet and visible spectral regions with Al_2O_3 *Thin Solid Films* **518** 4935–40
[66] Gao L, Lemarchand F and Lequime M 2013 Refractive index determination of SiO_2 layer in the UV/Vis/NIR range: spectrophotometric reverse engineering on single and bi-layer designs *J. Eur. Opt. Soc. Rapid Publ.* **8** 13010
[67] Snowden C 1998 *Introduction to Semiconductor Device Modelling* (Singapore: World Scientific)
[68] Grundmann M 2015 *The Physics of Semiconductors: an Introduction Including Nanophysics and Applications* (Berlin: Springer)
[69] Shockley W and Read W T Jr 1952 Statistics of the recombinations of holes and electrons *Phys. Rev.* **87** 835–42
[70] Hall R N 1952 Electron–hole recombination in germanium *Phys. Rev.* **87** 387
[71] Markowich P A, Ringhofer C A and Schmeiser C 1990 *Semiconductor Equations* (Berlin: Springer)
[72] Black L E, Allen T, McIntosh K R and Cuevas A 2014 Effect of boron concentration on recombination at the p-Si–Al_2O_3 interface *J. Appl. Phys.* **115** 093707
[73] Nelder J A and Mead R 1965 A simplex method for function minimization *Comput. J.* **7** 308–13
[74] Wilson M, Lagowski J, Jastrzebski L, Savtchouk A and Faifer V 2001 COCOS (corona oxide characterization of semiconductor) non-contact metrology for gate dielectrics *Characterization and Metrology for ULSI Technology: Int. Conf. (Gaithersburg, Maryland, USA)* (*AIP Conf. Proc.* vol 550) pp 220–5
[75] Schroder D K 2002 Contactless surface charge semiconductor characterization *Mater. Sci. Eng.* B **91** 196–210
[76] Kasap S O 2001 *Thermoelectric Effects in Metals: Thermocouples* (e-booklet) (Saskatoon: University of Saskatchewan)
[77] Boivin L 1993 Automated absolute and relative spectral linearity measurements on photovoltaic detectors *Metrologia* **30** 355–60
[78] Fischer J and Fu L 1993 Photodiode nonlinearity measurement with an intensity stabilized laser as a radiation source *Appl. Opt.* **32** 4187–90
[79] Kübarsepp T, Haapalinna A, Kärhä P and Ikonen E 1998 Nonlinearity measurements of silicon photodetectors *Appl. Opt.* **37** 2716–22
[80] Stock K, Morozova S, Liedquist L and Hofer H 1998 Nonlinearity of the quantum efficiency of Si reflection trap detectors at 633 nm *Metrologia* **35** 451–4